Planarized nanophotonic sensor for real-time fluid sensing

Liu, Yazhao; Salemink, H. W.M.

DOI
10.1063/1.4993104

Publication date
2017

Document Version
Final published version

Published in
AIP Advances

Planarized nanophotonic sensor for real-time fluid sensing

Yazhao Liu[1] and H. W. M. Salemink[1,2,a]
[1]*Faculty of Civil Engineering and Geosciences, Petroleum Engineering, Delft University of Technology, Stevinweg 1, 2628 CN Delft, The Netherlands*
[2]*Institute for Molecules and Materials, Radboud University Nijmegen, Heijendaalseweg 135, 6525 AJ Nijmegen, The Netherlands*

(Received 16 January 2017; accepted 28 August 2017; published online 11 September 2017)

A planarized on-chip nanophotonic sensor based on a photonic crystal cavity is realized in this work. The sensor was embedded in a solid protecting material (flowable oxide) with perfect filled holes: this eliminates problems of fouling in practical applications. The functional area of the sensor is created by carefully removing the protecting material only on the top surface of the cavity. A wavelength shift of 7.5 nm was observed in experiment which is very close to a simulation result of 9.0 nm for sensing water (n=1.33) and crude oil (n=1.45) samples. Swift and accurate sensing was verified by a real-time dynamic measurement with rapidly alternating analytes in a microfluid channel. [http://dx.doi.org/10.1063/1.4993104]

Fast and accurate sensing is a prime goal of environmental monitoring and bio/chemical diagnosis. Due to the development of nano-fabrication techniques, sizes of sensors have been remarkably reduced to a few microns or even to sub-micron scale. Tiny sensors made on small chips can now perform similar functions as classic large-sized sensors do, but with much less energy-consumption.[1,2] Among nano-scale sensors, all-optical sensors are of great interest for their immunity to electrical interference. The working principles of these sensors rely on variations of optical response as surrounding media are changed.[3,4] Specific properties, such as resonant wavelength, can be traced in sensing. In our recent works, we have focused on photonic-crystal-cavity-based all-optical sensors for several reasons. First, photonic crystal sensors feature an especially small footprint and high quality factor/volume,[5–9] which can meet the requirement of limited quantities of analytes. Secondly, photonic crystal can be fabricated accurately by electron-beam lithography and dry-etching in a very short time. A large scale and cost-effective manufacturing may be realized by using existing fabrication techniques.

In our previous works, we have designed and realized sensors with enhanced light-matter-interaction,[10,11] and we have also optimized a cavity for high-refractive-index liquid sensing.[12] Here we present our research on a planarized photonic crystal sensor, which aims at a very important issue of preventing fouling in real applications. Unlike previous designs of photonic crystals with open holes,[10–14] the planarized sensor is embedded in a solid protecting medium with an exposed surface of functional area only. Since the sensor is well protected, solid or colloid-like particles cannot block the holes, and the intrinsic properties of the sensor are less susceptible to fouling than sensors with open holes. The sensing ability of this embedded sensor was tested in real-time measurements of alternating fluid in experiment.

The structure of the photonic crystal cavity is illustrated in Fig. 1. The investigated structure consists of holes being plasma-dry-etched through a silicon slab and its refractive index n_{slab} is 3.4. The photonic crystal has a triangular lattice. A cavity is created by skipping three holes in the Γ-K direction. The cavity is surrounded by 10 rows of holes in the Γ-K direction, and 12 rows of holes in

[a]Corresponding author: H.Salemink@science.ru.nl.

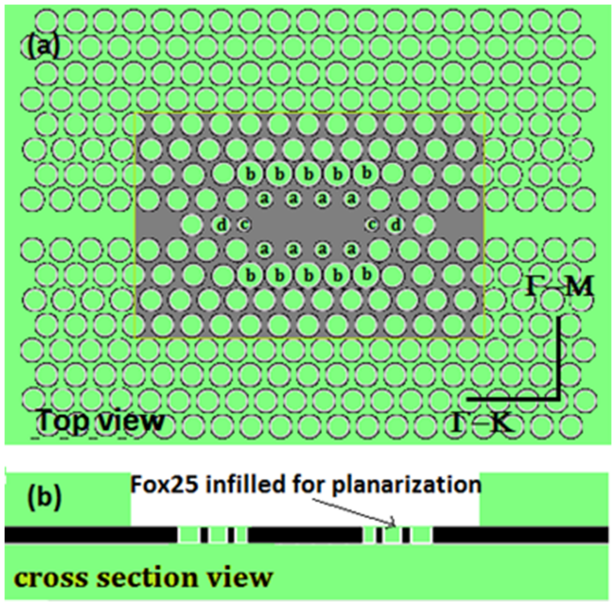

FIG. 1. (a) Top view of the cavity-design. Lattice constant a, radius r, $r = 0.35a$. $r_a = 0.7$r, $r_b = 1.18r$ with $\Delta y_b = 0.04a$, $r_c = 0.56r$ with $\Delta x_c = 0.21a$, and $r_d = 0.84r$. (b) Cross section view of the cavity with the flowable-oxide-planarization.

the Γ-M direction. Different from designs of photonic crystals we have published before, the entire silicon cavity is planarized and well protected, by the underneath silicon-dioxide and by a cured flowable oxide (Fox-25). The protecting medium Fox-25 fills holes of the photonic crystal and forms a planarized surface as shown in the side view of Fig. 1(b) with an ellipsometer-measured refractive index of 1.45. The silicon-dioxide layer underneath the film has a refractive index of 1.46. Design of the planarized sensor started from optimized holes and slab-thickness. The radii and thickness of the holes are set as $r/a = 0.35$, $h/a = 0.44$ (a is the lattice constant of the photonic crystal). Light confinement in the horizontal direction is calculated by using three-dimensional finite different time domain (FDTD) simulation program of MEEP.[15,16] A broadband pulse is placed inside the cavity as a TE-polarized dipole point source with Gaussian frequency distribution to excite intrinsic cavity modes. We decouple the optical fields into individual sinusoids and calculate the decay rates of H_z component after 400 calculation-steps after excitation.[17] In our calculation, the intrinsic resonance of the cavity appears at frequencies of 0.308 (a/λ) with a quality factor of ~1900. Resonant light is confined not only in the cavity but also extends to two neighbouring rows as shown in the inset of Fig. 2(a). This area of light confinement is the actual functional part of the planarized nanophotonic sensor.

We expose this functional area by opening an access from the protecting medium, but still keep the holes filled by precise controlling of dry-etching of the protecting medium. Sensing-ability is described by transmission spectra. We choose structural parameters as follows: $a = 500$ nm, $h = 220$ nm. Two neighboring rows of the cavity are slightly moved 10 and 20 nm away from the centre in the Γ–M direction. The radii of the first neighbouring row is $r_a = 122$ nm and the radii of the second row is $r_b = 206$ nm. Two pairs of holes next to the centre are also modified in the Γ–K *direction.* The nearest pair of holes is shifted 105 nm outwardly and reduced to $r_c = 100$ nm. The next pair also has reduced radii of $r_d = 147$ nm. A pair of single-mode photonic crystal waveguides serves as the light input/output waveguides. Figure 2(a) illustrates the wavelength shift of this planarized sensor in contact with two analytes. Water and oil, of which refractive indices are set to be 1.33 and 1.5 respectively, cover the entire planarized sensor in the simulation. Two peaks in black and red correspond to water and oil resonances. For water contact, resonance appears at 1550 nm. For oil contact, the resonance wavelength is red shifted by 9 nm to 1559 nm, which shows a sensitivity of 52.9 nm/RIU (refractive index unit). Compared to our previous design with open holes,[12] which had a simulated wavelength shift of 10.4 nm between water/oil, the wavelength shift in this planarized

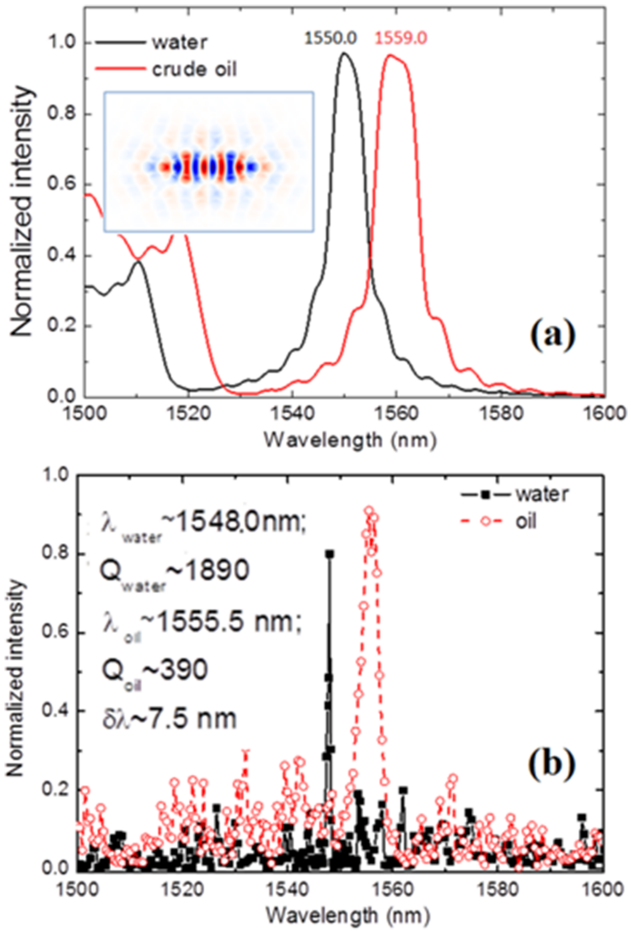

FIG. 2. (a) The calculated transmission spectra of the sensor with flowable-oxide-planarization for water/oil sensing. A change in refractive index of $\Delta n = 0.17$ (RIU) between water and oil results in a spectral shift of 9.0 nm. The inset shows the electric field distribution of the resonant mode around frequency $f = 0.308$ (a/λ) in the simulation. (b) Experimental transmission spectra of the sensor. The black and red spots were data measured for water and oil contact. A change in refractive index of $\Delta n \sim 0.14$ between water and crude oil sample results in a spectral shift of 7.5 nm.

sensor is nearly identical. The light-matter-interaction on the surface of the planarized sensor is not significantly weakened by the filled holes in the functional area. The filled holes of the photonic crystal enable optical and mechanical stability, and make the sensor less susceptible to fouling by debris or stuck residues. We also think it will enable a better surface for sensitizing layers in molecular selective applications.

The nanophotonic sensor was fabricated on silicon-on-insulator (SOI) wafer with a 220 nm-thick silicon slab and a 3 μm-thick silicon dioxide insulator-layer below the slab. As presented in the flowchart of Fig. 3(a), a 200 nm-thick Ebeam-resist (ARP6200.09) is spun on a clean chip and subsequently the pattern of the sensor was written by a Leica EBPG 5200 e-beam lithography system operating at 100 keV. After lithography and pattern-development, the exposed region of the SOI wafer were dry-etched by Alcatel AMS100 system with gas flows of SF_6 and O_2 at -120°C. An example of an etched photonic crystal is shown in Fig. 3(b). Afterwards, the entire chip was covered and filled by the flowable oxide of Fox-25 by a spinner at room temperature. The flowable oxide remains liquid in this step, thus provided a flat surface on the chip. The whole chip was then post-baked at 300°C for 1 hour then cured by exposing to electrons from a SEM, which transformed Fox-25 from liquid to a solid silica-like structure. The transformed layer of Fox-25 had good endurance to mechanical breakages. No clear marks were found after moderately scratching the chip with sharp tips of tweezers. Next, an aligned dry-etching was precisely applied to open the access atop the cavity.

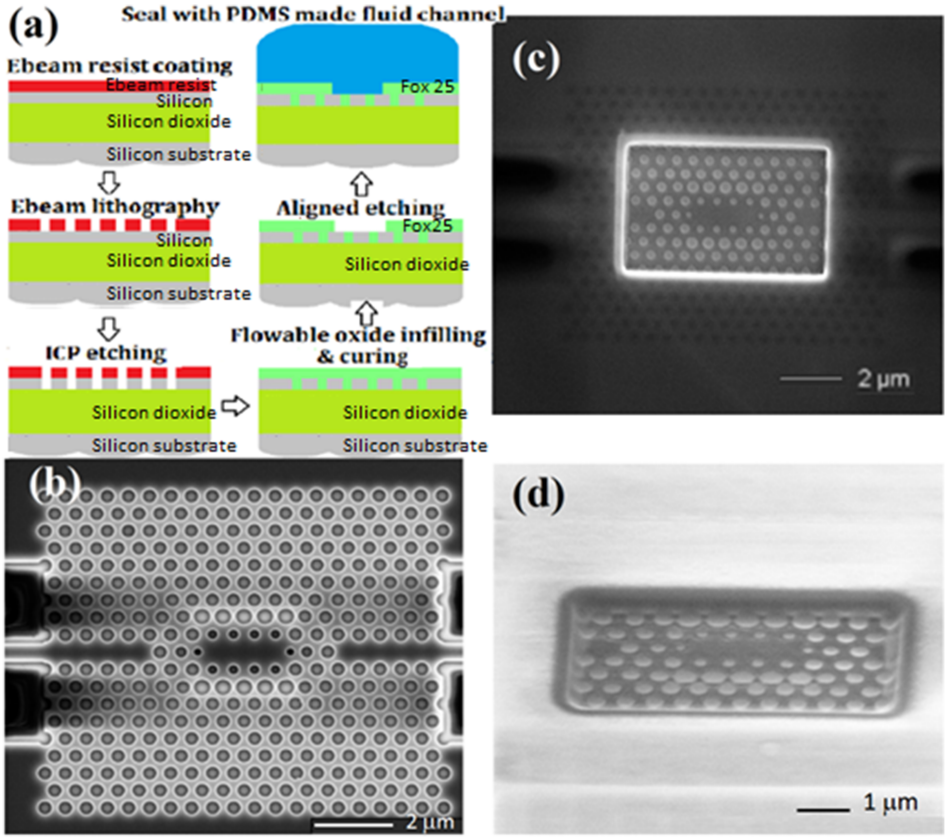

FIG. 3. (a) A flowchart of planarized-sensor-fabrication. (b) A scanning electron microscope (SEM) image of the photonic crystal after SF_6 and O_2 dry-etching. (c), (d) SEM images of the sensor with a carefully opened access on the cured Fox-25 protection layer. Fox-25 has been infiltrated in the holes and on the top, and made the surface of the sensor flat. The liquid-access was opened by aligned etching which stopped at the top surface of the silicon slab. Therefore the holes in this area were still filled with Fox-25.

The etching rate was controlled well to approximately stop at the top of the silicon slab and create a smooth surface for the functional area as presented in Fig. 3(c), 3(d). A fluid channel made of PDMS (Polydimethylsiloxane) was peeled away from a deep-etched silicon mold. Bonding of the fluid channel on the sensor chip was carried by oxygen-plasma treatment followed by a post-bake at 160°C for 1 hour to enhance the bonding strength.

For the transmission measurements, light was coupled into and coupled out of the sensor via a pair of tapered stripe waveguides. In order to minimize the mode mismatch, the stripe waveguides were tapered from 2.5 μm in width at edges to 866 nm at the joints of the photonic crystal waveguides. Both waveguides were exposed to outside by cleaving at edges. A tunable laser (Yenista Tunics T100S-HP) ranging from 1500 to 1680 nm served as the light source. TE polarization-maintained lensed fibers were used to couple light into and out of the waveguides. Finally, the output fiber was connected with a sensitive photodetector and a power meter.

The transmission spectra of static analytes were measured firstly and plotted in Fig. 2(b). Crude oil sample tested in experiments had an average refractive index of 1.47 as measured by a near-infrared refractometer. Water sample with a refractive index of 1.33 was taken directly from an ordinary water tap. Liquid drops were placed on top of the sensor chip by syringe needles to realize static measurements. The black spectrum in Fig. 2(b), which corresponded to water-contact, shows a resonance around 1548 nm with a Q factor of 1890. The Q factor we observed here is very close to the simulation result of 1900. The red spectrum is obtained with oil contact, and its Q factor is 390 at 1555.5 nm. The wavelength shift of 7.5 nm between water and oil showed a sensitivity of 53.6 nm/RIU, which is very close to our simulation result of 52.9 nm/RIU. It should be noted that the oil samples

used in the experiment are crude oil, which usually contained multi-hydrocarbon compositions. The reduction in quality factor for the oil is a result of multiple indices of refraction. The compositions expanded the range of refractive indices (which was also observed from the refractometer), and resulted in a broader resonance than liquids with pure composition, such as water. Reflected in the spectra, this feature induced a lower Q factor of crude oil than that of water.

Real-time dynamic sensing was investigated by using flow-rate controllers: syringe pumps. Programmable syringe pumps served as reservoirs of water and oil, and were connected to the two input ports of the PDMS made fluid channel through pipelines. At a T-junction of the two input ports, water droplets were generated in the fluid channel due to surface tension and were pushed toward the sensor by the flow. Periodicity and size of droplets can be controlled by syringe pumps. The experimental set-up and a microscope-photo of a water droplet in the oil flow are illustrated in Fig. 4(a), 4(b).

We fixed the input light at the resonant wavelength of oil-contact at 1555 nm, and recorded the output intensity of the sensor as analytes flowed inside the channel. Oil and water alternatingly contacted the sensor on its top surface via periodical flowing droplets. Under this dynamic process, we expected high intensity whenever the sensor is in contact with oil, and low intensity for anytime of water-contact, as the signal at the oil related wavelength rides up and down in intensity. The dynamic sensing process was monitored and recorded by a camera from a microscope mounted above the chip and viewing through the transparent PDMS channel. A dynamic video clip of the sensing process is presented in Fig. 5 (Multimedia view).

The output intensity of dynamic sensing for about 3 minutes is plotted in Fig. 6. Rectangular regions with red borders are time of oil-contact read from the video clip recorded by the camera. Gaps among these are time of water-contact. Alternating time between oil and water droplets was about

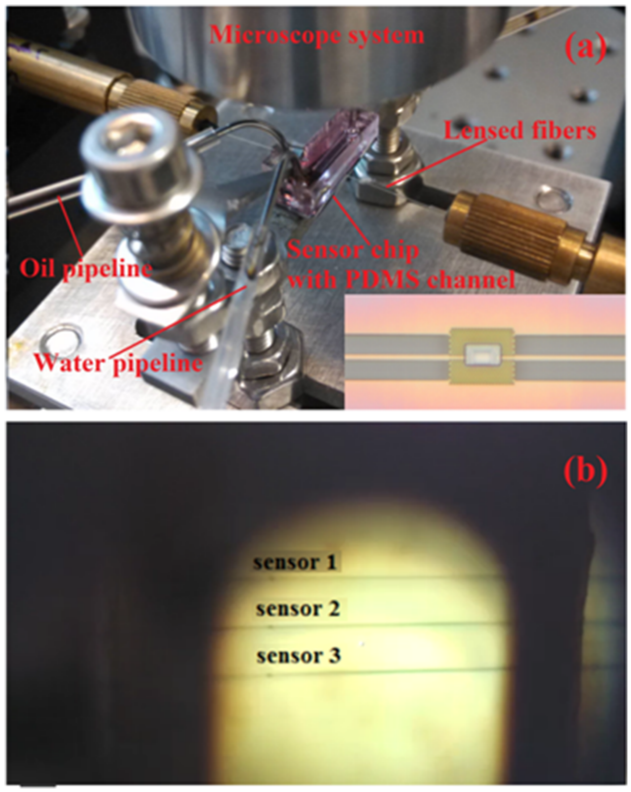

FIG. 4. (a) The experimental set-up for real-time sensing. Two pipelines on the left side of the setting injected water and oil. A third pipeline collected waste on the other side. The pink block in the center of the figure is the PDMS made fluid channel. The planarized sensor as shown in the inset located below the channel. (b) A top-view from the microscope through the PDMS channel. Three cavities and access waveguides are viewed. A water droplet in the oil flow covered the sensor from top. The clear bubble is water, and the black background in the channel is crude oil.

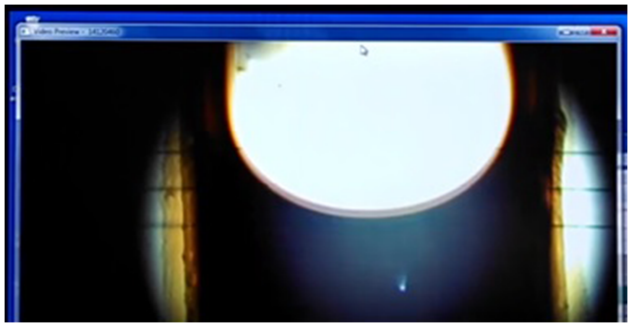

FIG. 5. A dynamic video clip of water droplets flowing with crude oil in the PDMS fluid channel. Droplets contacted the planarized sensor from top. (Multimedia view) [URL: http://dx.doi.org/10.1063/1.4993104.1]

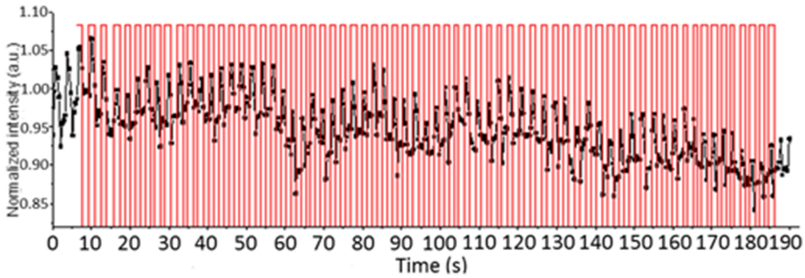

FIG. 6. The output intensity of the sensor at oil-resonant-wavelength in the dynamic sensing with alternating analyte-droplet contact. The high values were from oil-contacts and the low values were from the water-contacts.

1 second. The flow velocity was about 1.67 mm/s. The original data of output intensity of the sensor is marked as the solid black symbols and connected by a black line in Fig. 6. Even with the limited time-resolution of our photodetector (Agilent 8164A Lightwave Measurement System) of ~ 0.2 s and a slight decline of output power caused by a mechanical drift of the lensed fibers, the periodic change in output signal is still very obvious. By collating time-axis of video clip and dynamic output intensity, a very good match was achieved. Each peak of intensity corresponded to an oil-contact, and each bottom coincided with a contact of the sensor with a water droplet. Comparing Fig. 6 to Fig. 2(b), the intensity-contrast between water and oil in the dynamic alternating droplet-sensing is smaller than that in the static single-analyte measurement. We attribute this phenomenon to an oil-wetted surface of the cured Fox-25, which was also observed on the chip with a slightly darkened color caused by oil-wetting. Quantitative analysis of the oil-wetting was applied by simulating transmission spectra of the sensor with thin films of residual oil covering the surface of Fox-25 as illustrated in Fig. 7(a). We adjust the thickness of the residual oil film from 0 to 880 nm. Variations of resonances were calculated in Fig. 7(b). For oil films with thickness thicker than 400 nm, resonances were almost located at the same wavelength around 1560 nm. While thinner oil films have large shifts in their resonant wavelengths. Therefore at the fixed wavelength of 1560 nm (marked by the black arrow as the simulated oil resonance), output intensities of the sensor with thinner oil films vary dramatically from 0.1 to 0.9 within 110 nm range of film-thickness. Average intensity-drop from oil-contact to water-contact in Fig. 6 is ~10%, thus we presume that the residual oil film on the surface of Fox-25 had a thickness about 100 to 110 nm in our experiment. From another experiments, we have verified that the thickness of residual oil film is flow velocity and analyte-ratio depended. Intensity-drop from oil-contact to water-contact had been increased to more than 95% with larger water ratio and higher flow velocities up to 150 mm/s. This work will be discussed separately in a future paper.

In summary, a planarized nanophotonic sensor was realized by embedding photonic crystals in a protecting material of cured Flowable oxide (Fox-25). The light-matter-interaction between analytes and confined light in the sensor was enabled by a carefully exposed functional area above

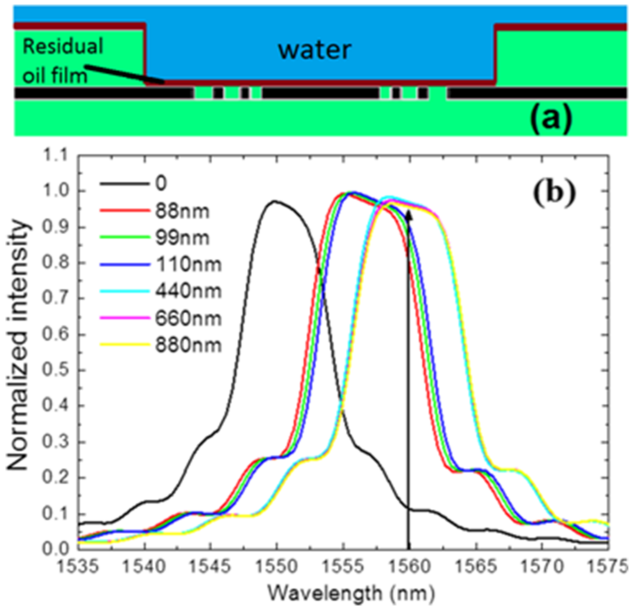

FIG. 7. (a) Cross-section view and (b) simulated spectra of the sensor with a residual oil film on the top surface of the Fox-25. Note the strong wavelength shift for film thickness up to 440 nm.

the planarized sensor. Functionalities of this planarized nanophotonic sensor were verified by static and dynamic flow measurements, using alternating oil and water droplets. This type of small, planarized nanophotonic sensors can be of importance to practical applications in fields of environment monitoring and biological/medical detection.

This work is supported by Shell Global Solutions: NanoPhotonic Sensors (NPS), and partially by the KNAW China Exchange Program 530-5CDP19. Many appreciations are given to Juun van der Horst, Cor Kruijsdijk from Shell E&P, William Rossen, Jan-Dirk Jansen, and Michiel Slob from Delft University of Technology, and Tonnie Toonen from Radboud University.

[1] J. Homola, S. Yee, and G. Gauglitz, Sens. Actuators B **54**, 3–15 (1999).
[2] R. Boyd and J. Heebner, Appl. Opt. **40**, 5742–5747 (2001).
[3] M. Adams, G. A. DeRose, M. Loncar, and A. Scherer, J. Vac. Sci. & Technol. B **23**(6), 3168–3173 (2005).
[4] O. Levi, M. M. Lee, J. Zhang, V. Lousse, S. R. J. Brueck, S. Fan, and J. S. Harris, Proc. SPIE **6447**, 64470P (2007).
[5] Y. Akahane, T. Asano, B.-S. Song, and S. Noda, Nature **425**(6961), 944–947 (2003).
[6] Y. Akahane, T. Asano, B.-S. Song, and S. Noda, Optics. Express **13**(4), 1202–1214 (2005).
[7] B.-S. Song, S. Noda, T. Asano, and Y. Akahane, Nature. Mate Material. **4**(3), 207–210 (2005).
[8] T. Asano, B.-S. Song, and S. Noda, Optics Express **14**(5), 1996–2002 (2006).
[9] T. Tanabe, M. Notomi, and E. Kuramochi, Electronics Letters **43**, 3 (2007).
[10] Y. Liu and H. Salemink, Opt. Express **20**(18), 19912–19920 (2012).
[11] Y. Liu and H. W. M. Salemink, "All-optical on-chip sensor for high refractive index sensing," Appl. Phys. Let. **106**, 031116 (2015).
[12] Y. Liu and H. W. M. Salemink, Europhys. Lett. **107**, 34008 (2014).
[13] N. A. Mortensen, S. S. Xiao, and J. Pedersen, Microfluid. Nanofluid. **4**(1-2), 117 (2008).
[14] C. Kang, C. T. Phare, Y. A. Vlasov, S. Assefa, and S. M. Weiss, Optics Express **18**(26), 27930 (2010).
[15] J.-P. Berenger, J. Comput. Phys. **114**(2), 185–200 (1994).
[16] http://ab-initio.mit.edu/wiki/index.php/Meep.
[17] V. A. Mandelshtam and H. S. Taylor, J. Chem. Phys. **107**(17), 6756–6770 (1997).